PAPER • OPEN ACCESS

Gross and net erosion balance of plasma-facing materials in full-W tokamaks

View the article online for updates and enhancements.

Gross and net erosion balance of plasma-facing materials in full-W tokamaks

A. Hakola[1,*] ⬤, J. Likonen[1], A. Lahtinen[2], T. Vuoriheimo[2] ⬤, M. Groth[3] ⬤,
H. Kumpulainen[3] ⬤, M. Balden[4] ⬤, K. Krieger[4] ⬤, M. Mayer[4] ⬤,
T. Schwarz-Selinger[4] ⬤, S. Brezinsek[5] ⬤, M. Kelemen[6], S. Markelj[6] ⬤,
M. Barac[7], S. Gouasmia[7] ⬤, I. Bogdanovic Radovic[7] ⬤, A. Uccello[8] ⬤,
E. Vassallo[8] ⬤, D. Dellasega[8,9] ⬤, M. Passoni[8,9] ⬤, M. Sala[9] ⬤, E. Bernard[10] ⬤,
M. Diez[10] ⬤, C. Guillemaut[10], E. Tsitrone[10], the ASDEX Upgrade Team[a],
the EUROfusion MST1 Team[b] and the EUROfusion WP PFC Contributors[c]

[1] VTT, PO Box 1000, 02044 VTT, Finland
[2] Department of Physics, University of Helsinki, Helsinki, Finland
[3] Department of Applied Physics, Aalto University, Espoo, Finland
[4] Max-Planck-Institut für Plasmaphysik, Garching, Germany
[5] Institut für Energie und Klimaforschung-Plasmaphysik, Forschungszentrum Jülich, Jülich, Germany
[6] Jožef Stefan Institute, Ljubljana, Slovenia
[7] Ruder Boskovic Institute, Zagreb, Croatia
[8] Istituto per la Scienza e Tecnologia dei Plasmi CNR, Milan, Italy
[9] Department of Energy, Politecnico di Milano, Milan, Italy
[10] CEA, IRFM, Saint-Paul-lez-Durance, France

E-mail: antti.hakola@vtt.fi

CrossMark

Abstract
Gross and net erosion of tungsten (W) and other plasma-facing materials in the divertor region
have been investigated in deuterium (D) and helium (He) plasmas during dedicated
experiments in L- and H-mode on ASDEX Upgrade and after full-length experimental
campaigns on the WEST tokamak. Net erosion was determined via post-exposure analyses of
plasma-exposed samples and full-size wall components, and we conclude that the same
approach is applicable to gross erosion if marker structures with sub-millimeter dimensions
are used to eliminate the contribution of prompt re-deposition. In H-mode plasmas, gross
erosion during ELMs may exceed the situation in inter-ELM conditions by 1–2 orders of
magnitude while net erosion is typically higher by a factor of 2–3. The largest impact on net
erosion is attributed to the electron temperature while the role of the impurity mixtures is
weaker, even though both on ASDEX Upgrade and WEST significant amounts of impurities
are present in the edge plasmas. Impurities, on the other hand, will lead to the formation of
thick co-deposited layers. We have also noted that with increasing surface roughness, net
erosion is strongly suppressed and the growth of co-deposited layers is enhanced. In He

plasmas, gross erosion is increased compared to D due to the higher mass and charge states of the plasma particles, resulting from larger energies due to sheath acceleration, but strong impurity fluxes can result in apparent net deposition in the divertor. Our results from ASDEX Upgrade and WEST are comparable and indicate typical net-erosion rates of 0.1–0.4 nm s^{-1}, excluding the immediate vicinity of the strike-point regions.

(Some figures may appear in colour only in the online journal)

1. Introduction

Tungsten (W) and tungsten-based alloys are promising candidate materials for plasma-facing components (PFCs) in future fusion reactors [1–3], largely due to their small erosion yields by physical sputtering, high melting point and large thermal conductivity, as well as low retention of radioactive tritium (T) and other hydrogen isotopes of the plasma fuel in W. Understanding the physics mechanisms influencing erosion and retention behaviour of tungsten PFCs has been high in the priority list of the European fusion research programme under the EUROfusion Consortium, both with the help of dedicated experiments and using interpretative numerical simulations [4]. In this contribution, we report on recent experimental activities related to distinguishing the balance between the gross and net erosion of W in a tokamak, i.e. how material is primarily released into the edge plasma via sputtering and how it is subsequently migrating and re-depositing in the reactor vessel. We focus on the low-field-side (outer) strike point (OSP) area of the divertor where large heat and particle fluxes will result in considerable plasma-wall interactions. The data is collected from two medium-sized, full-W European tokamaks, ASDEX Upgrade (AUG) [5] and WEST [6], and can be compared to results from JET with its ITER-like material mix of a Be first wall and a W divertor [7].

Gross erosion of W is traditionally determined with the help of spectroscopic measurements, by recording the intensity of selected neutral (and ionized) W spectral lines in different locations of the vessel during a series of plasma discharges, while to assess the amount of net erosion, a number of PFCs has to be removed from the device for post-exposure surface analyses. Usually, these wall structures have become available only after a full-length experimental campaign, consisting of several different plasma scenarios and configurations. Despite these limitations, the following global conclusions have been drawn, see [7–10]:

- In a full-W device, net erosion of W PFCs during a typical experimental campaign will not cause insurmountable issues for the component lifetime, excluding the regions most heavily impacted by plasma exposure in the divertor. Data from AUG [8] indicate net erosion of W being <0.1 nm s^{-1}, excluding the exact OSP area. In a future high duty-cycle reactor, however, even such values are unacceptable stressing the need for detached divertor operations.

- Erosion of PFCs is strongly dependent on local plasma conditions and transients impinging on them. Especially, the role of edge localized modes (ELMs) on W sputtering is estimated to be >50% [7, 9]. In a reactor, plasma operations with strongly mitigated or suppressed ELMs is thus required to keep PFCs intact and mitigate the erosion sources of W.

- The resulting erosion patterns can be significantly altered by long-range migration of material, even turning areas with considerable gross erosion into net-deposition regions.

- Impurities will enhance sputtering but can also result in the formation of thick, co-deposited layers which can be rich in W, thus complicating determining the actual erosion rates of the original PFC material.

To provide further insights into erosion behaviour during individual discharges and to provide a benchmarking dataset for subsequent modelling, AUG is equipped with an upgraded divertor manipulator (DIM-II) [11] since 2014. DIM-II allows exposing a variety of test samples, or even full-scale wall tiles, to a number of pre-determined plasma discharges in the OSP region (i.e. only minor changes were made to the plasma parameters during the sample exposure) and analysing the outcomes shortly after the experiment. In the last couple of years, DIM-II has been used to investigate erosion mechanisms in plasmas ranging from low-power L-mode to high-performance H-mode, both in deuterium (D) and helium (He), and using samples with varying geometries, materials, and surface morphologies, see [12–16]. An extensive database is available for simulation efforts, consisting of a combination of plasma-wall-interaction codes, such as ERO [17], SOLPS-ITER [18], DIVIMP [19], and WallDYN [20].

On WEST, erosion investigations were initiated in 2016 by equipping several divertor PFCs with marker coatings and exposing them to plasmas during successive campaigns (labelled C1–C5), consisting of a variety of L-mode plasmas in D and He (the latter only in C4) [21]. The marker tiles have recently become available for post-exposure analyses, enabling for the first time a comparison between campaign-integrated erosion investigations in different plasma gases. In addition, numerical simulations have been initiated using the ERO2.0 [22] and SolEdge2D-EIRENE [23] codes.

Section 2 will give a detailed description of the samples used, the plasma experiments on which the results are based, and the measurements carried out. In section 3, the obtained
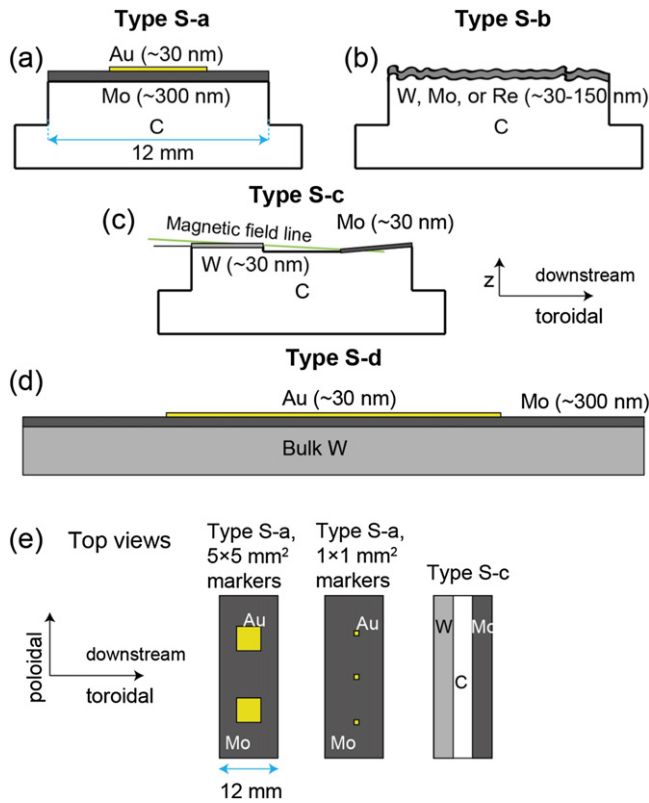
Figure 1. Schematic drawings of the different sample types used in the AUG experiments: (*a*)–(*d*) side views, (*e*) top views of sample types S-a and S-c.

AUG results will be presented while section 4 focuses on the first data gathered from experiments on WEST. Section 5 reviews the status of modelling activities and, finally, conclusions are drawn in section 6.

2. Experimental erosion investigations on ASDEX Upgrade and WEST

2.1. ASDEX Upgrade experiments using the divertor manipulator DIM-II

On AUG, the DIM-II divertor manipulator has been used for gross- and net-erosion investigations during four dedicated experimental sessions in D and two in He, covering both L- and H-mode plasma scenarios [12–16] and such that only minor variations were made to the plasma parameters during each experiment. For each experiment, a number of small samples (surface area 33.5×12 mm^2, see figure 1) with marker coatings were mounted on dedicated target tiles that fitted into the divertor geometry of AUG. As marker materials, we used W or proxies to it—molybdenum (Mo), gold (Au), and rhenium (Re)—to better evaluate the erosion and re-deposition of the actual markers, without the disturbing effect induced by the long-range migration of eroded W in a full-W device. For the substrate, we typically selected graphite to ease experimental determination of changes in the thickness of the coatings.

The applied sample types can be categorized as follows:

(a) Type S-a, graphite samples with a Mo marker layer (thickness $\sim$300 nm) and Au marker spots (target value for thickness $\sim$30 nm, dimensions 1×1 mm^2 and 5×5 mm^2) on top. The surface roughness in terms of the arithmetical mean deviation was typically $R_a \sim 1~\mu$m but in experiment E3 (see below) smoother substrates with $R_a \sim 0.2~\mu$m were used. The small spots were designed for gross-erosion studies, the larger ones for assessing net erosion.

(b) Type S-b, graphite samples with varying morphologies and W, Mo, or Re marker layers (thickness 30–150 nm). The surface roughness varied from $R_a \sim 0.004~\mu$m to $R_a > 2~\mu$m, including also the 'standard' value of $R_a \sim 1~\mu$m to provide a benchmarking case for comparing the results obtained from type S-a and S-c samples introduced above and below.

(c) Type S-c, graphite samples with a W marker coating (thickness $\sim$30 nm), a recessed uncoated trench (depth $\sim$0.2 mm), and an inclined area with a Mo marker coating (thickness $\sim$30 nm). The surface roughness was $R_a \sim 1~\mu$m. Deposition at the bottom of the trench was used to estimate prompt re-deposition.

(d) Type S-d, bulk W tile (dimensions $\sim$230 $\times$ 80 mm^2) with a Mo marker coating ($\sim$300 nm) and an Au stripe (width $\sim$30 mm, thickness $\sim$30 nm). The surface roughness was $R_a \sim 0.2$–0.3 μm.

Schematic drawing of the samples can be found in figure 1 and photos of them mounted on the target tiles for different experiments in figure 2. A short summary of the experiments can be found below and additional details in table 1.

(a) Experiment E1, L-mode plasmas in D with a high electron temperature (T_e) at the OSP. Two separate sessions have taken place: the first one, called E1A, with W-coated roughness samples (type S-b) and trench samples (type S-c) and the second one, referred to as E1B, with Au marker samples (type S-a) and Mo-coated roughness samples (type S-b). The samples were inserted in four rows in the poloidal direction, on two target tiles toroidally next to each other as figures 2(*a*) and (*b*) show. The electron temperature T_e reached values up to 20–30 eV at the OSP and the overall exposure time (in terms of the flat-top time of the discharge) varied from 32 s (in E1B) to 80 s (for E1A) such that measurable erosion and re-deposition patterns would result [12, 15, 16].

(b) Experiment E2, H-mode plasmas in D exhibiting large type-I ELMs with a frequency of $\sim$50 Hz and an energy loss of $\sim$20 kJ. In this experiment, one target tile was equipped with Au marker samples (type S-a) while the other tile was of type S-d, see figure 2(*c*). The electron temperature was comparable to that in the L-mode experiments but due to strong erosion, the exposure only lasted for $\sim$6 s.

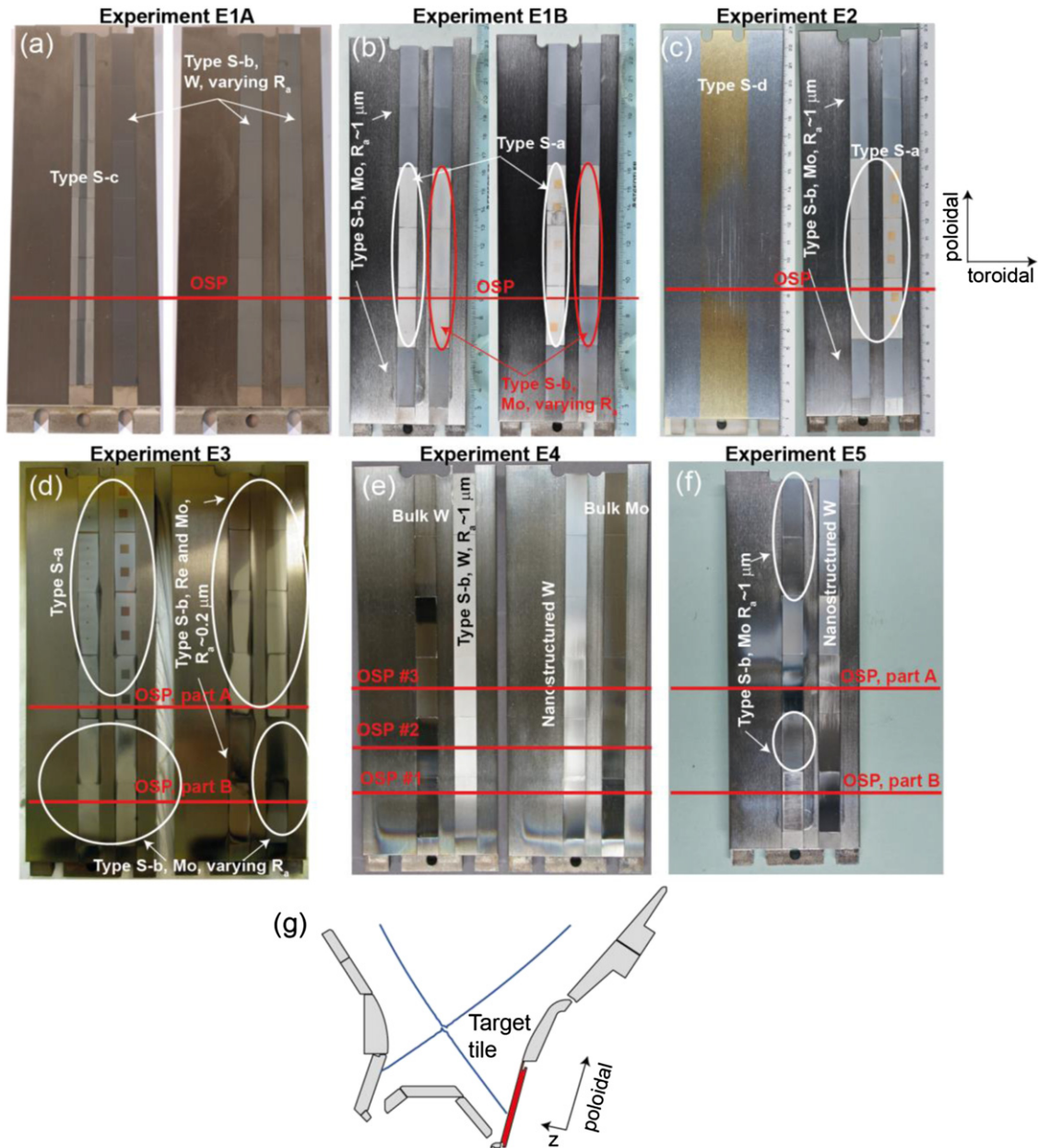(c) Experiment E3, H-mode plasmas in D with small (energy loss $\sim$10 kJ) and frequent (frequency $\sim$125 Hz) ELMs

Figure 2. (*a*)–(*f*) Photographs of the marker samples, mounted on the DIM-II target tiles (dimensions ∼230 × 80 mm^2) for the different erosion experiments on AUG. Here, (*a*) refers to experiment E1A, (*b*) to experiment E1B, (*c*) to experiment E2, (*d*) to experiment E3, (*e*) to experiment E4 and (*f*) to experiments E5A and E5B. The OSP positions are marked using red lines and the sample types are as described in figure 1; (*g*) Illustration of the AUG divertor geometry and the position of the DIM-II target tiles during experiment E1B.

and using samples of types S-a and S-b. Two sessions were carried out, with the OSP being located either on the gold marker samples or on the Mo-coated roughness samples (see figure 2(*d*)). The analyses of the exposed samples have only started, and the results will be reported elsewhere.

(d) Experiment E4, ELMy H-mode plasmas in He. The erosion investigations were conducted parasitically to the main experiment where the growth and destruction of nanostructures (W fuzz) on pre-modified W surfaces was studied and with three different OSP positions [13, 14]. A full poloidal row of W-coated graphite samples

(type S-b, coating thickness 30 nm, $R_a \sim 1$ μm) was used for extracting the erosion profiles of W, see figure 2(*e*) for details.

(e) Experiment E5, a combination of ELMy H-mode (session E5A) and L-mode (session E5B) plasma exposures in He with smaller impurity contents of the plasma than in experiment E4 [24]. The two sessions corresponded to different OSP positions according to figure 2(*f*). Erosion data was obtained from Mo marker coatings (type S-b, coating thickness ∼100 nm, $R_a \sim 1$ μm), poloidally located between the two OSPs and in the far scrape-off layer (SOL) ∼50 mm off from the uppermost OSP.

Table 1. Key parameters of the different AUG experiments. Here ECRH stands for electron cyclotron resonance heating, ICRH is ion cyclotron resonance heating, and NBI is an acronym for neutral beam injection.

Experiment	Experiment type and AUG discharges	Gas	Plasma current (MA)/ Toroidal field (T)	Core density ($\times 10^{19}$ m^{-3})	Heating power (MW)	Exposure time (s)	ELM frequency (Hz)/ energy loss (MJ)
E1A	L-mode #31238–#31251	D	0.8/2.5	~2.0	1.3 (ECRH)	~80	—
E1B	L-mode #35609–#35617	D	0.8/2.5	~4.0	0.7 (ECRH)	~28	—
E2	H-mode, large ELMs #36410–#36415	D	1.0/2.4	~9.0	3.3 (ECRH)	~6	~50/~20
E3	H-mode, small ELMs #38069–#38073	D	0.6/2.5	~8.5	4.0 (ECRH) + 5.0 (NBI)	~15	~125/~10
E4	H-mode, 3 OSPs #32642–#32666	He	0.8/2.5	~9.5	2.6 (ECRH) + 3.9 (ICRH) + 2.1 (NBI)	~100 (OSP1) ~ 60 (OSP2) ~ 10 (OSP 3)	~130/~ 10–20
E5A	H-mode #36671–#36681	He	0.8/2.5	~9.0	3.4 (ECRH) + 5.3 (NBI)	~70	~200/ ~15–25
E5B	L-mode #36682–#36689	He	0.8/2.5	~6.5	1.3 (ECRH)	~36	— ~15–25

The equilibrium of the applied plasma discharges did not vary dramatically from one experiment to another, mainly the OSP position was altered within 40–50 mm. A typical example of the magnetic configuration, corresponding to that of experiment E1B, is shown in figure 2(*g*) together with the position of the exposed samples. The OSP ion flux density in the L-mode cases was $j_{sat} \sim (1.5–2.0) \times 10^{22}$ m^{-2} s^{-1}, while in H-mode plasmas it was $j_{sat} \sim (1.0–2.5) \times 10^{23}$ m^{-2} s^{-1}.

After the experiments, all samples were analysed using Rutherford backscattering spectrometry (RBS) and nuclear reaction analysis (NRA) to determine changes in the thickness of the different marker coatings and deposition of various elements on them or in their immediate vicinity. Both broad-beam (beam size 1–2 mm^2) and microbeam (beam size 10×10 μm^2, scanned across an area of 500×500 μm^2) measurements were carried out. Additional data on erosion and deposition patterns were provided by scanning electron microscopy (SEM), energy dispersive x-ray spectroscopy (EDX), confocal laser scanning microscopy and particle induced x-ray emission (PIXE), especially for the samples with the small Au marker spots.

2.2. WEST experiments in the different campaigns

On WEST, W sputtering has been investigated both in D and He, during dedicated sessions in the C3 and C4 campaigns. In C3, only D plasmas were used while in the last weeks of C4, WEST was exclusively operated in He plasmas [25]. The results of W gross erosion in D are reviewed in [26] whereas the corresponding He data will be published elsewhere but is briefly summarized in section 4.2. The erosion studies in D were predominantly carried out in a series of lower hybrid (LH) heated L-mode discharges ($I_p = 0.5$ MA, $B_t = 3.6$ T, $n_e = 1–4 \times 10^{19}$ m^{-3}, $P_{LH} = 0.8–3$ MW) where a broad parameter scan was performed in terms of the divertor plasma temperature (inner divertor <10 eV, outer divertor up to 50 eV), impurity flux and composition, as well as the position and rate of plasma fuelling.

Net erosion, for its part, relied on the post-exposure analyses of marker tiles installed in the vessel before the C1 campaign in 2016 and then removing a subset of them both after the C3 and the C4 campaigns [21]. The marker tiles were made of graphite, then covered with Mo (target value for thickness ~3 μm) and W (~12 μm) coatings and finally with a 100 nm thick Mo and 1–2 μm thick W marker layers (according to RBS analyses in the mm^2 scale) on top. A schematic illustration of the marker tiles as well as a photo of two of them (C3-22o and C3-34i) after being exposed during the C3 campaign of WEST are shown in figure 3. The analyses of the marker tiles is an extensive effort by several European research labs and, as of now, the first broad-beam RBS and NRA measurements have been completed (similar settings applied as for the AUG samples, see section 2.1) to obtain the overall erosion and re-deposition patterns on the marker tiles. More detailed investigations using SEM, EDX, PIXE, focused ion beam cross-sections on microscopic scales, and secondary ion mass spectrometry have also started.

Figure 3. (*a*) Schematic illustration of the produced layer configuration on the marker tiles exposed during the WEST C3 and C4 campaigns. ((*b*) and (*c*)) Photographs of two marker tiles removed from the (*b*) outer (tile C3-22o) and (*c*) inner (tile C3-34i) divertors of WEST after its C3 campaign.
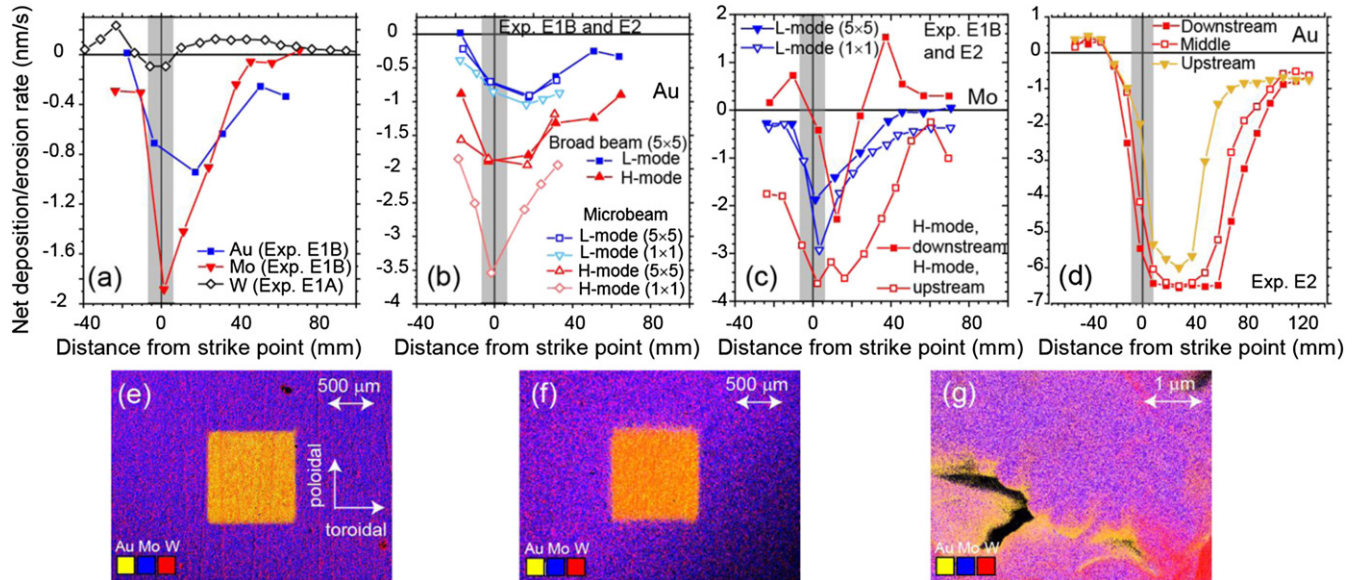

Figure 4. (*a*)–(*d*) Net deposition/erosion rates (positive/negative values) of AUG marker samples as a function of poloidal distance from the applied OSP; (*a*) comparison between Au (5×5 mm^2), Mo, and W markers in L-mode (experiments E1A and E1B); (*b*) comparison between 1×1 mm^2 and 5×5 mm^2 Au markers in L- and H-mode (experiments E1B and E2), data from both broad-beam and microbeam measurements is included; (*c*) comparison between Mo markers after exposure in L- and H-mode (experiments E1B and E2); (*d*) comparison between different toroidal locations of the wide Au marker stripe in H-mode (experiment E2). (*e*)–(*g*) EDX images of the 2D elemental maps of Au, Mo, and W for (*e*) a 1×1 mm^2 Au spot after experiment E1B (L-mode) in the vicinity of the OSP, (*f*) for an Au spot at a corresponding location after experiment E2 (H-mode) and (*g*) a higher magnification image from the surroundings of the spot in (*f*) at $\sim$0.5 mm toroidally downstream from it. The coordinate directions are the same in (*e*)–(*g*).

3. Overview of ASDEX Upgrade results

3.1. Comparison between L- and H-mode erosion data

3.1.1. L-mode experiments. The general feature in both the L- and H-mode discharges is that the experimentally determined net-erosion curves peak around the OSP, roughly following the shape of the T_e profile. This can be most clearly demonstrated for the two L-mode experiments (experiments E1A and E1B) in figure 4(*a*), which shows the evaluated net-erosion rates for the marker materials Au, Mo, and W (all having comparable surface roughness of $\sim$1 μm) as a function of the poloidal distance along the target-tile surface. For W, the net-erosion maximum is in the range of 0.1–0.2 nm s^{-1}, while Au exhibits 3–5 times higher and Mo up to 15 times larger erosion rates. Notice that in the case of Au, no sample was located at the exact OSP position, thus the values in figure 4(*a*) may underestimate the actual net-erosion peak as also hinted by the results of numerical simulations in [16].

Another interesting observation is the striking difference from the campaign-integrated data [8], highlighting the importance of re-deposition processes in the strike-point area. During extended plasma operations, covering a variety of L- and H-mode scenarios, the apparent net erosion of W can be decreased by a factor of 10 from the L-mode values reported above and the difference between the erosion rates of Mo and W may shrink down to 2–3 compared with the value of 15 mentioned above [27]. Possible reasons for these are that during an extended campaign of plasma operations, the strike-point positions as well as the electron temperature profiles are different from discharge to discharge, altering the balance between erosion and deposition in the poloidal (and sometimes in the toroidal) direction. Typically, erosion peaks become less prominent while thicker and more complex deposited layers are observed. Operations with a mixture of impurities and regular vessel conditioning can further amplify the formation of the deposits in the divertor region, issues that were on purpose eliminated in the experiments reported here.

An additional difference between W and its proxies are the noticeable net-deposition peaks that W shows on both sides of the OSP, a sharp one in the private-flux region (PFR) and a broader but shallower one some 10–60 mm on the SOL side of the strike-point area. The origin of the peaks is connected with long-range migration of eroded material from adjacent regions [15], even from the main chamber of AUG, and the hypothesis is supported by the complete absence of net deposition on the analyzed Au and Mo markers.

The primarily eroded particles are locally re-deposited in the immediate vicinity of their origin, at distances <1 mm. To assess the toroidal (or poloidal) extent of re-deposition, microbeam PIXE analyses as well as EDX measurements were performed around the different Au marker spots. None of the applied techniques was able to detect any signs of gold outside of their origin (see figure 4(*e*) as an example), which is in accordance with our ERO simulations indicating an exponentially decreasing tail of deposited particles within the first centimeter from their origin [16].

The gross erosion in L-mode was spectroscopically determined to be around 0.2–0.3 nm s^{-1} for W [12] and to an order of magnitude higher for Mo [16]. These are in line with the reported differences in net-erosion rates mentioned above, indicating that for all the materials net/gross erosion ratio in our high-T_e experiments remains <0.5; the higher the electron temperature, the lower this ratio would be. Post-exposure analyses of the trench samples (type S-c) give estimates for both net erosion and re-deposition of W (at the bottom of the trench) and result in a higher net/gross-erosion ratio of 0.6–0.7 However, here the data are distorted by additional deposition of material from the plasma [12].

Comparison between the small (1 × 1 mm^2) and large (5 × 5 mm^2) Au markers in figure 4(*b*) shows a clear difference between their erosion profiles: small markers are eroded at 10%–20% higher rates throughout the analyzed poloidal region. If the small markers were only showing the results of primary sputtering (thus gross erosion) and the data from the larger markers was representative of net erosion, the net/gross-erosion ratio would become 0.8–0.9 around the OSP, even higher than the values above. This hints towards a requirement for sub-millimeter-size dimensions for the small markers such that the effect of re-deposition could be eliminated. Additional support is coming from our ERO simulations in [16]: the contribution of re-deposition drops from >50% to <40% with the characteristic marker dimension decreasing from 5 to 1 mm. Similar conclusions have been made from a corresponding experiment (marker samples with varying dimensions exposed to L-mode plasmas in the divertor region) in DIII-D: for larger samples re-deposition fraction is typically 40%–70% while for mm-sized markers, <10% have been measured to become re-deposited [28]. ERO simulations from several devices (DIII-D, JET-ILW, EAST) also prove that the overall re-deposition can reach values of 90%–100% in high-density plasmas while in low-density conditions reduction down to 50% was obtained [28–30].

3.1.2. H-mode experiments. In the H-mode experiment with large type-I ELMs (experiment E2), the inter-ELM conditions were comparable to those in the L-mode. Based on spectroscopic measurements, gross erosion was amplified by one or two orders of magnitude compared to the case in L-mode, an observation that can be largely attributed to the occurrence of ELMs. Switching to H-mode led also to an increased net-erosion rate but this was not as dramatic as was the case for gross erosion (see figures 4(*b*) and (*c*). For Au, net erosion was 2–4 times more intense in H-mode whereas in the case of Mo the difference was only around a factor of 1.5 in favour of H-mode but with large variations in the toroidal direction.

For the small Au markers, the difference in erosion rates between the L- and H-mode was the largest and they also showed the most peaked profiles around the OSP. With the same assumptions as in the L-mode case, the net/gross-erosion ratio was evaluated to <0.5 in the strike-point region while it increased to >0.6 at distances >15 mm from it. This implies that, in regions where the transient heat loads are significant, material migration can be drastically different from the case in more benign L-mode conditions.

The results for Mo in figure 4(*c*) also show that in H-mode material migration is considerable, as evidenced by the shift of the main erosion peak further into the SOL (by 10–15 mm) and the appearance of deposition-dominated areas poloidally both on the PFR and SOL sides of the main strike point. This is most noticeable for markers located toroidally 15–20 mm more downstream from the first ones (comparison between the S-a samples with small and big Au marker spots, see figure 2(*c*)), indicating that eroded Mo may migrate much longer distances than was the case in L-mode in section 3.1.1. We speculate this to be due to long-range transport of the eroded material, possibly by successive erosion–deposition steps. In addition, one has to keep in mind that in H-mode conditions more material is released, thus also more of it can be toroidally transported and caught by ion-beam measurements, i.e. exceed the sensitivity threshold.

Similar conclusions on the enhanced migration of the eroded material in H-mode can be drawn for gold, which exhibited measurable deposition in between and around the 1 × 1 mm^2 and 5 × 5 mm^2 marker spots and with comparable surface densities. In addition to the actual marker spots, part of the deposited gold in these surrounding regions might have originated from the tile with the broad marker stripe, located upstream of the type S-a samples (see figure 2(*c*)). If this was the case, the eroded gold would have travelled a distance of >100 mm before being deposited. EDX analyses of the vicinity of the Au marker spots (examples shown in figures 4(*f*) and (*g*) give further insights into the deposition and migration picture. Outside of the original markers, gold was found deposited together with W and following the sample topography such that the most noticeable inventories were in deep grooves of the surface. Such behaviour is not dependent on the type of the experiment but first analyses of Au markers after the small-ELM experiment E3 produce similar results.

The poloidal erosion profiles on the bulk tile with a wide Au marker stripe (type S-d), shown in figure 4(*d*), indicate

that in H-mode the entire marker can be damaged and completely eroded at the OSP, thus explaining why target material can be found in measurable amounts even on adjacent tiles in the toroidal direction. Notice that the entire coating was damaged and the substrate underneath was revealed, thus the true erosion rate can be much larger than the $\sim$6.5 nm s^{-1} that figure 4(*d*) indicates. The more downstream the erosion measurements along the Au stripe were made, the more noticeable the erosion was, thus re-deposition does not always compensate for strong sputtering as was noticed for the Mo markers in figure 4(*c*). This particular tile was also used for spectroscopic measurements of gross erosion of Au, and the radiance of the selected Au I spectral lines was at least 20 times stronger than that of W. This way an upper limit could be set to the gross-erosion rate in H-mode, that being several hundreds of nanometers per second. The behavior of the bulk tile can also be due to its surface state as discussed in section 3.2.

3.2. Effect of surface morphology on erosion and deposition profiles

Increasing surface roughness results in reduced net erosion of W, up to a factor of 5–10 when the roughness changes from $R_a \sim 0.3$ μm to >3 μm as can be seen from figure 5(*a*). Here, the data is obtained from type S-b samples, exposed to L-mode plasmas of experiment E1A [31]. Interestingly, when moving only one decay length ($\sim$10–20 mm) away from the strike point, net erosion changes into strong net deposition as the roughness exceeds the value of $\sim$1 μm. The deposition peaks co-inside with the regions where ERO simulations predict the eroded particles being driven by the $\mathbf{E} \times \mathbf{B}$ drift [15], accompanied by the strong influx of material from the surrounding areas.

Additional information on the role of roughness was obtained by measuring the erosion of the Mo coatings on samples with different roughness values, from $R_a \sim 0.004$ μm to 2 μm (experiment E1B) and they confirm the conclusions above: the rougher the surface, the smaller is the net erosion (see figure 5(*a*)). In addition, EDX analyses indicate that on rough surfaces large amounts of W and impurities are deposited (according to figure 5(*b*)) while on smoother surfaces only remnants of the original coating (refer to figure 5(*c*)) are left close to the OSP. In figure 5(*c*), the dominant blue color means that the original coating has largely vanished, not to be mixed with the formation of carbon-rich co-deposited layers.

A puzzling observation is that Mo coatings in between the Au marker spots ($R_a \sim 1$ μm) seemed to be more susceptible to erosion—more than a factor of two—than the ones on the actual roughness samples with the same R_a value, albeit the nominal plasma and impurity fluxes were the same. We speculate this to be caused by the different toroidal locations of the samples. According to figure 2(*b*), the roughness samples were either located more downstream than the Au marker samples or mounted on the second target tile where the magnetic field angle deviates from that on the first tile, resulting in more significant re-deposition. Moreover, the structure of the coating might have been different despite them exhibiting the same
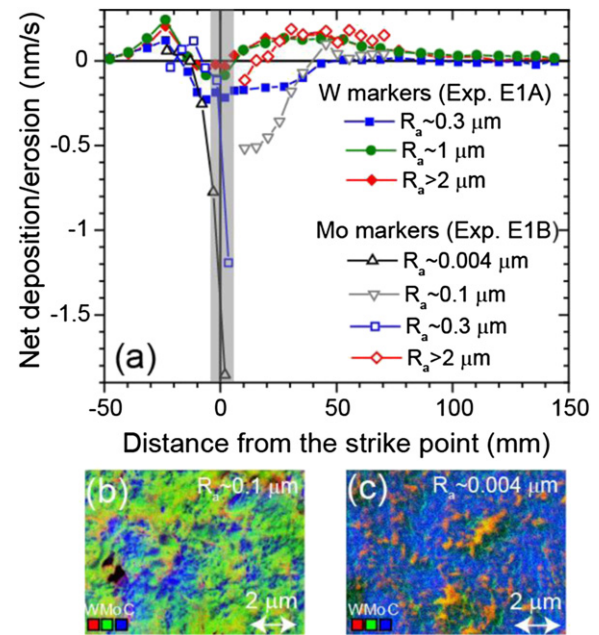

Figure 5. (*a*) Net deposition/erosion (positive/negative values) of W and Mo marker coatings with different surface roughness exposed to D plasmas in L-mode (experiments E1A and E1B). ((*b*) and (*c*)) EDX images of the 2D elemental maps of C, Mo, and W after experiment E1B. In (*b*), data from a medium rough ($R_a \sim 0.1$ μm) Mo marker at the OSP is shown while in (*c*) the corresponding data for a smooth sample ($R_a \sim 0.004$ μm) at the OSP is reproduced.

average roughness in terms of R_a: the Mo coatings in between the Au spots were produced by arc-discharge sputtering, the Mo coatings on the roughness samples by pulsed laser deposition. Based on the results, we stress that morphology cannot be described by a single parameter but more detailed analyses of the surface features are required.

Gross erosion of similar Mo-coated roughness samples as those discussed above was also investigated by exposing them to a low impact-energy ($E_{in} \sim 90$ eV) helium plasma beam in the linear plasma device PSI-2 [32]. The *effective sputtering yield*, i.e. the fraction of primarily eroded particles that are not readily trapped by neighboring surface features, was shown to be reduced with the roughness by 30%–40%. Moreover, erosion was preferentially occurring at the highest surface peaks. Thereby, the higher the surface roughness, the more ill-defined concept average gross erosion becomes but erosion and re-deposition should be treated in the microscopic scale [33–35]. Our earlier results from an AUG experiment where a W-coated Mo marker tile with a melt-damaged spot was exposed to H-mode plasmas, provide a clear evidence on the local nature of erosion and re-deposition phenomena [36]. Net erosion up to complete removal of the W marker layer at elevated parts of the surface, oriented towards the incident plasma flux, was measured while corresponding shadowed areas showed net deposition. In contrast, on the undamaged areas with a relatively smooth surface, uniform erosion patterns, determined by the incident plasma parameters, at length scales larger than the different surface features was measured. One therefore needs to carefully consider the surface features

and their evolution during plasma operations to obtain a reliable estimate for the net/gross-erosion balance. Initially rough surfaces in erosion-dominated areas can become smoother during their exposure by plasma impact, thus potentially altering the erosion/deposition balance [37].

The actual roughness samples exposed to H-mode plasmas (in experiment E3) are still unanalyzed, but the first hints for the impact of roughness and morphology on Au erosion in H-mode are obtained from the analyses of relatively rough surfaces (sample S-a, $R_a \sim 1 \ \mu m$) and of their smoother counterparts (sample S-d, $R_a \sim 0.2$–$0.3 \ \mu m$) following experiment E2. On smooth surfaces, complete removal of the coating may result in the OSP region (figure 4(*d*)) and only in the far SOL, net erosion approaches the values measured for the rougher samples (figure 4(*b*)). Considering originally intact and properly aligned PFCs with a typical roughness ranging from one to several micrometers, there will thus be no insurmountable showstopper for their usage in a fusion reactor from the erosion point of view. However, the situation may be completely different if the components are damaged or misaligned, and under such conditions the PFC lifetime can be largely compromised.

3.3. Comparing PFC material erosion in D and He

In helium plasmas, W erosion is intensified by the large mass and charge of the plasma species. Additionally, if the plasmas are heated using ICRH, a large influx of material from the main chamber to the divertor will result [13]. The role of strong deposition became evident in the first H-mode experiment in He (experiment E4): even though the conditions were favorable for boosting erosion at the OSP—especially the electron temperature was $T_e > 20$ eV—only thick deposited layers were found on the material surfaces, see figure 6(*a*). One could argue that poloidal shifts of the OSP during the experiment (altogether three different positions) have resulted in overcompensation of any erosion peak during the subsequent phase but this kind of process would not have led to the net-deposition profile being as smooth as figure 6(*a*) shows. In addition, the proximity of the experiment to a boronization on AUG may have led to considerable amounts of impurities, including boron, carbon (from erosion of W-coated wall components), oxygen, and deuterium (from previously formed co-deposited layers) in the SOL plasma. As a result, thick co-deposits at the divertor region are formed [14].

The extra main-chamber W source was eliminated in experiment E5 by using only NBI and ECRH for plasma heating, in addition to which the impurity content of the edge plasma was minimized by carrying out the discharges far from a boronization, but otherwise aiming at exceeding the thresholds needed for forming or destroying W nanostructures [24]. The analyzed Mo marker coatings showed two characteristic regions in the poloidal direction: in between the strike points set for the L- and H-mode parts of experiment E5 (gray bars in figure 6(*a*)), net deposition was observed while in the far SOL, prominent net erosion was measured.

The calculated net-erosion rates in figure 6(*a*) are constant but smaller than those derived for D experiments (see figure 4), and change into apparent net deposition the closer one moves
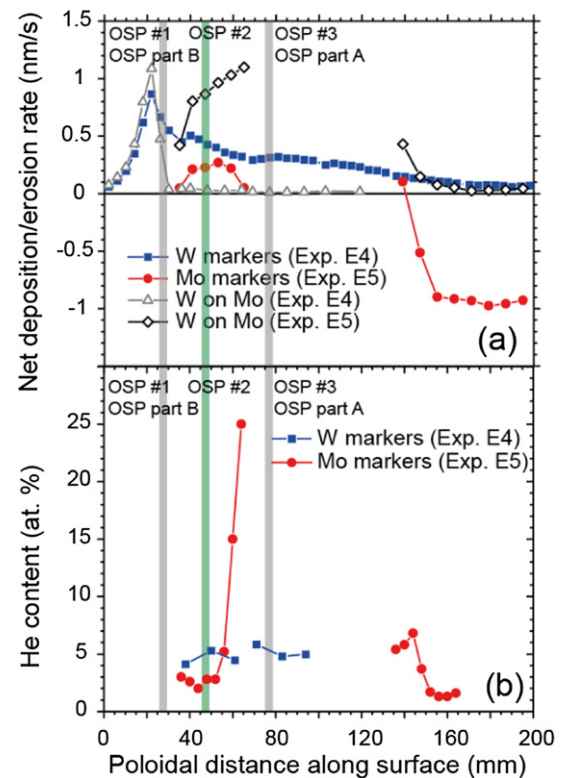

Figure 6. (*a*) Net deposition/erosion (positive/negative values) of W and Mo markers exposed to He plasmas in H-mode in experiments E4 and E5. Also the deposition of W on Mo markers is shown. The gray and green bars mark the poloidal locations of the OSPs applied in the two experiments, the upper row (OSP#1, #2, #3) stands for E4, the lower row (OSP part A and B) for E5. (*b*) Analyzed He content of the W and Mo marker samples after experiments E4 and E5.

to the uppermost OSP. This can again be attributed to the **E** × **B** drift. The shape of the erosion profile is the subject of future investigations but one factor could be connected to the entire Mo layer being damaged during the experiment, thus the numbers in figure 6(*a*) may only show the lower limit for the erosion of bulk components.

An additional observation is that more W is deposited on Mo surfaces after experiment E5 than after E4. A potential reason to this is connected with the surface quality of the materials: in experiment E4 bulk Mo samples with a relatively smooth surface were used while in experiment E5 the roughness of the Mo markers was $R_a \sim 1 \ \mu m$. The results are therefore in line with what is reported after D experiments in section 3.2. Worth noticing is that the deposition patterns of W on Mo qualitatively agree with the determined retention profiles of He as figure 6(*b*) proves. The retention peak around 50–60 mm can be connected with co-deposition since, according to figure 6(*a*), the particular region in experiment E5 is strongly dominated by deposition while this is not the case in experiment E4.

3.4. Deposition and migration of impurities in D and He

Compositional analyses of the layers deposited on the different marker samples provide further insights into how material is migrating in the edge plasma, both in D and He. In L-mode
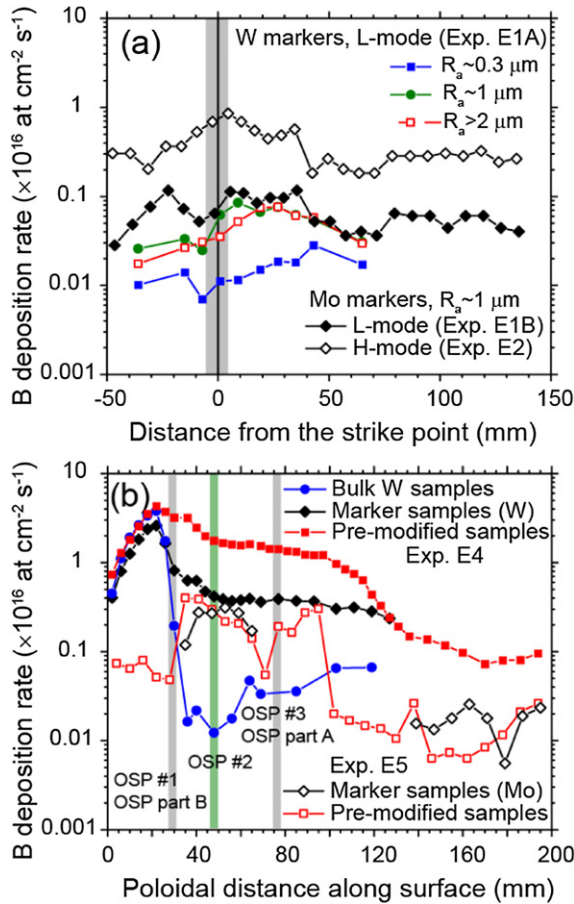
Figure 7. Deposition rates of B for W and Mo marker samples (*a*) with different surface roughness exposed to D plasmas (experiments E1A, E1B, and E2) and (*b*) with different surface morphology following exposure to He (experiments E4 and E5). The gray and green bars mark the poloidal locations of the OSPs applied in the two experiments, the upper row (OSP#1, #2, #3) stands for E4, the lower row (OSP part A and B) for E5. Here, the bulk W samples were the smoothest ($R_a \sim 0.2$–0.3 μm) and pre-modified samples the roughest (R_a several μm); for the marker samples $R_a \sim 1$ μm.

D plasmas, net-deposition profiles of the main light impurities boron (shown in figure 7(*a*)), carbon, and nitrogen are in line with the deposition peaks of W in Figure 5(*a*), in addition to which smooth samples show less deposition than the rough ones, by the same fraction of about 5–10 than the difference in their net-erosion rates. Based on the L-mode experiments E1A and E1B, no big differences exist between Mo and W marker coatings as long as the surface roughnesses are comparable. In the PFR, somewhat less B can be observed after the second experiment (on Mo) but this may be connected with the details of the experiment and better coverage of analyses in the PFR region.

In the H-mode experiment E2 in D, almost an order of magnitude higher B deposition rates are obtained than in L-mode and the main deposition peak is symmetric with respect to the OSP. However, the saturation values for the B concentrations may have not yet been reached due to the short duration ($\sim$6 s) of the experiment.

In He, for its part, the exposure times were generally of the order of 100–200 s and according to figure 7(*b*), the deposition

profiles of impurities such as that of B are qualitatively similar to the corresponding ones for W and He (referring to figure 6). In experiment E5, minimizing extra W and impurity sources during the experiments resulted in also suppressing deposition by a factor of 2–3 and the almost complete absence of elements like D and C with respect to experiment E4. Comparison between experiments E2 and E5 in H-mode indicates no noticeable differences in the deposition of B, suggesting that the migration of impurities in different plasma gases in otherwise identical conditions is similar.

Analogously to the case in D, deposition of impurities in He plasmas is more prominent on samples with a rough or highly modified surface, as can be seen from the comparison between bulk W surfaces ($R_a \sim 0.2$–0.3 μm), W marker coatings ($R_a \sim 1$ μm) and W samples with pre-modified surfaces (consisting of nanoscale structures) in figure 7(*b*). The roughness effect appears to be missing in the PFR and in the far SOL, in the former case due to the thick co-deposits that make the surface topographies to resemble each other after a few discharges and in the latter case due to the small amount of material available to be deposited.

4. First results for divertor erosion on WEST

4.1. Erosion in deuterium

The spectroscopically measured gross erosion during a series of representative ohmic and L-mode D plasma discharges in WEST was determined to be 1–2×10^{20} s^{-1} in the C3 campaign [26]. These are in line with the observations from the AUG divertor during its first experimental campaign in a full-W device without boronizations [9], however, the WEST data is taken from the high-field (inner) side of the divertor. The main impurities in the performed discharges appeared to be carbon and oxygen, the latter being quite prominent in the plasma with concentrations up to 3 at.%, based on analysis of the exhaust gas and spectroscopy. On AUG, in contrast, carbon is the most noticeable light impurity element together with boron (from boronizations but mainly in the main chamber) and nitrogen (from regular seeding experiments) and resulting in an impurity mix comparable to that in WEST in terms of W sputtering.

Net-erosion investigations in D have recently begun and the results will be discussed in [21]. Results for the erosion of the topmost W layer are also collected in figure 8 for the two marker tiles C3-22o and C3-34i (exposure time $\sim$7300 s) introduced in figure 3, together with the deposition patterns of B, C, and O on the markers. The data indicate little erosion outside of the exact strike-point regions, both on the inner and outer side of the vessel. Especially on the inner side (tile C3-34i), thick deposits ($>$10 μm) have been measured next to the strike point. No well-defined marker coating can be recognized anymore but a layer consisting of the marker materials (W and Mo) as well as impurities, including metallic ones, has formed. Similar observations have been made on AUG over the course of several campaigns with durations of 2600–6600 s, see [8]. On the outer side (tile C3-22o), a more classical picture of erosion- and deposition-dominated areas is visible: complete erosion of the markers at the exact strike point location, and a region with
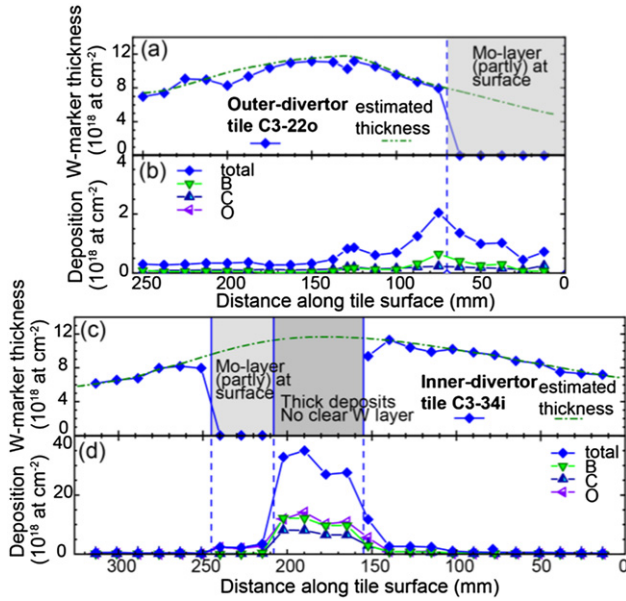
Figure 8. (*a*) Thickness of the remaining W marker on the outer-divertor tile C3-22o (see figure 3) as a function of distance along the tile surface. Here 1 μm corresponds to $\sim 6.3 \times 10^{18}$ at cm^{-2} (assuming the density of bulk W) and the green line represents the estimated thickness profile of the coating before plasma exposure. (*b*) Deposition of different elements (B, C, and O) on tile C3-22o. (*c*) Thickness of the remaining marker on the inner-divertor tile C3-34i. (*d*) Deposition of different elements on tile C3-34i. Notice the different *y*-axis scales in (*b*) and (*d*).

deposited impurities some 20–50 mm off from it. All this will result in a lower limit for the estimated campaign-averaged net erosion, being ~ 0.1–0.4 nm s^{-1}.

4.2. Erosion in helium

In He plasmas, during the C4 campaign [25], the strength of the W source was somewhat surprisingly a factor of two lower than in corresponding discharges in D, even though the electron temperature at the divertor was relatively high (up to 20 eV). On the basis of results from AUG, this should have resulted in considerable material erosion. The reason can be associated with a low impurity content of the edge plasma, especially the C concentrations had dropped from what the situation in D was and this may be due to the lack of significant chemical sputtering. On the other hand, the source strength could be varied within a large margin, by 1–2 orders of magnitude, by applying *N* seeding during the discharges. Both in He and D, the W sources exhibited asymmetry between the inner and outer parts of the divertor [26]. With increasing plasma density, sputtering at the inner side first increased and then dropped to a small value while at the outer side erosion stayed at a constant level until the density became high enough, the threshold being somewhat larger in the case of He.

No clear data on the effect of He plasmas on W net erosion exist since half of the C4 campaign was devoted to continuing D plasma operations initiated in the C3 campaign. The main observations following C4 are that erosion around the strike points has started to extend over even larger areas than after

C3 and that the deposits have become thicker [21]. In addition, the deposition maximum in D has shifted further away from the inner or outer strike point.

5. Understanding erosion patterns by numerical simulations

As of now, modelling of the erosion data from AUG is ongoing while getting detailed insights into the physics mechanisms of the observed erosion patters in WEST has been left for the future, even though the work has been started. On AUG, the efforts have focused on applying the ERO code for the samples exposed at the OSP region, by concentrating on the L-mode experiments (experiment E1A and E1B) [15, 16]. The necessary background plasmas have been created using the onion-skin model of DIVIMP with the SOL option 22 activated and assuming the ion temperature being equal to the electron temperature, i.e. $T_i = T_e$. Option 22 refers to a case where, starting from given target conditions and including a wide variety of effects, a complete background plasma solution for density, ion and electron temperature, parallel flow velocity and parallel electric field can be generated. As such, the applied profiles have been able to give upper and lower boundaries for the true values of T_e and n_e. In addition, the anomalous diffusion coefficient $D_\perp$, the parallel-B electric field, and the impurity content of the plasma (in terms of B, C, N, and W concentrations) have been varied, the former in the range 0.2–1.0 m^2 s^{-1}. Recently, also SOLPS-ITER plasma backgrounds have become available but not yet applied for the erosion investigations in ERO.

Of the studied parameters, T_e has the largest impact on erosion, especially at the OSP: if the temperature is varied by less than a factor of two, net erosion values can be up to 2.5–3.0 times larger or smaller. Even small changes can be significant and the peaked nature of the applied T_e profiles has resulted in sharper erosion curves than what the experimental results indicate. This is noticeable since erosion is proportional to the incoming particle flux and the sputtering yield, the latter being strongly dependent on the electron temperature.

Another striking difference between the simulated and measured erosion profiles have been sharp net deposition peaks emerging on both sides of the OSP following ERO simulations. The higher the electron temperature is, the more prominent these peaks become. These have been associated with the $\mathbf{E} \times \mathbf{B}$ drift as already stated in section 3, ultimately shifting the gross erosion and deposition profiles with respect to each other. While drifts play a large role, cross-field diffusion is not significant, as evidenced by the very small value for $D_\perp$ that is required to reproduce experimental erosion profiles in low-density plasmas.

Concerning impurities, ERO simulations indicate that erosion is mainly dependent on the effective charge but not so much on the exact ratio of various light impurities (e.g. B, C, and N) in the SOL plasma. Furthermore, by varying the impurity content within the limits characteristic for discharges studied in this article, a small effect on the simulated profiles can be seen but only in regions where the electron temperature has dropped below 20 eV.

Particle-in-cell (PIC) simulations [15] further suggest that transport of material along the magnetic field lines has to be taken into account. Particles originating from other regions of the reactor vessel can travel several meters in the toroidal direction and accumulate in the divertor, typically in the PFR. Considering, on the other hand, the actual marker stripes or spots (Au or W), some 70% of the particles are deposited closer than 10 mm from their origin in the outer divertor, meaning that net-erosion patterns are a combination of local and global phenomena in the reactor. Similarly to the experiments, Au has been noticed to erode 3–5 times faster than W and the migration lengths for the two elements are comparable. Thus Au can be considered a suitable proxy for W in assessing its erosion and migration characteristics.

The main mechanisms behind gross and net erosion of W can thus be well reproduced by numerical simulations, enabling making predictions for erosion rates and material migration in future fusion reactors. However, further efforts are needed at least on the following fronts:

- The simulated profiles are typically much more peaked than the experimental ones. To this end, improved background plasma profiles are needed, especially in the strike-point regions, where both the electron temperature and density show large gradients as well as in regions where the validity of the $T_i = T_e$ assumption is questionable.

- The simulations indicate strong dependence of erosion rates on the size of the markers and such that small markers should show less erosion than their bigger counterparts. This is contrary to our observations (see figure 4) and could be connected to the too coarse grid applied in the simulations: re-deposition may show a much sharper profile than what the present modelling is able to catch.

- The complex combination of the marker and substrate materials in poloidal and toroidal directions has not been fully taken into account yet. This may have partly contributed to the largely underestimated net-erosion rates of Mo if one cannot resort to the assumption that the material layers are the same everywhere in the simulation volume.

- ELMs have not been included in the erosion simulations on AUG or WEST, requiring both inter- and intra-ELM phases to be handled separately.

Progress made in these topics will be reported in future publications.

6. Discussion and conclusions

The present paper has discussed the recent observations and results of PFC erosion in the two full-W European tokamaks AUG and WEST. While the WEST experiments have provided additional information on campaign-integrated erosion and deposition profiles of W to be compared with results from AUG, the AUG investigations have concentrated on understanding the role of various physics parameters on both gross and net erosion of different PFC materials during a series of pre-defined plasma discharges. In both devices, studies have been made in D and He, predominantly at the outer-divertor region where the largest heat and particle fluxes are expected. The main results can be summarized as follows:

- In addition to emission spectroscopy, gross erosion of PFC materials can be determined by measuring the erosion of specific marker coatings—provided that their dimensions are small enough (<1 mm) to minimize the contribution of prompt re-deposition. In low-density plasmas with high T_e, net/gross erosion can be >50%, while the role of re-deposition increases with increasing density.

- In H-mode plasmas, gross erosion during ELMs may exceed the situation in inter-ELM and L-mode conditions by 1–2 orders of magnitude while net erosion is typically higher only by a factor of 2–3. This corresponds to strong re-deposition of the sputtered material. Net erosion is largely influenced both by the electron temperature and the impurity concentration of the SOL plasma. For the experimental conditions studied here (high $T_e > 20$ eV, concentrations of light impurities $\leqslant 1.0$ at.%), net-erosion rates are most sensitive to small changes in T_e. Impurities, on the other hand, will lead to the formation of thick co-deposited layers, which are generally occurring poloidally on both sides of the actual strike-point region.

- The rougher the surface, the more will net erosion be suppressed and the thicker the co-deposited layers on the PFCs will be. Locally, net erosion will follow the surface topography such that in shadowed areas W re-deposition dominates while for plasma-exposed regions erosion is uniform at larger length scales than any microscopic feature on the surface. Roughness is therefore an essential parameter and a single roughness value (such as R_a) does not describe the full complexity of the sample topography [33].

- Based on results from AUG, in He plasmas gross erosion of W and other PFC materials is increased compared to the situation in D due to the higher mass and charge states of the impinging particles but, on the other hand, strong impurity fluxes at the divertor region can easily turn erosion into apparent net deposition. As the amount of impurities is reduced and excessive main chamber sputtering minimized, net erosion can be measured poloidally away from the OSP, up to the point where entire marker coatings have been worn out.

- On WEST, thick deposited layers (>10 μm) containing O, B, and W were measured on the high-field-side divertor after the C3 campaign, in the immediate vicinity of the erosion dominated strike-point area. This is comparable to what was found in AUG after several campaigns [38]. It will be of interest to monitor the evolution of these deposited layers and assess their potential impact on plasma operation if they reach a critical thickness.

- The data from AUG and WEST are very consistent when it comes to the gross erosion profiles and even the preliminary data on net-erosion patterns imply no big differences between the two devices. By combining the results, we obtain that in a variety of plasma conditions net erosion of W would be in the range 0.1–0.4 nm s^{-1} but in the OSP regions potentially larger values are expected.

Future studies will include detailed analysis of a new set of samples, which will provide us with additional data points for determining the impact of surface roughness on erosion as well as comparing the simulated migration patterns of trace elements to experimental observations.

Acknowledgments

ORCID iDs

A. Hakola https://orcid.org/0000-0003-1385-1296

T. Vuoriheimo https://orcid.org/0000-0003-4266-9178

M. Groth https://orcid.org/0000-0001-7397-1586

H. Kumpulainen https://orcid.org/0000-0003-1301-0497

M. Balden https://orcid.org/0000-0002-8755-9370

K. Krieger https://orcid.org/0000-0003-0427-8184

M. Mayer https://orcid.org/0000-0002-5337-6963

T. Schwarz-Selinger https://orcid.org/0000-0001-7461-2817

S. Brezinsek https://orcid.org/0000-0002-7213-3326

S. Markelj https://orcid.org/0000-0002-6603-4006

M. Barac https://orcid.org/0000-0002-9504-9522

S. Gouasmia https://orcid.org/0000-0001-6994-5668

I. Bogdanovic Radovic https://orcid.org/0000-0002-4100-736X

A. Uccello https://orcid.org/0000-0003-3044-1715

E. Vassallo https://orcid.org/0000-0001-8435-4196

D. Dellasega https://orcid.org/0000-0002-7389-9307

M. Passoni https://orcid.org/0000-0002-7844-3691

M. Sala https://orcid.org/0000-0002-6244-7612

E. Bernard https://orcid.org/0000-0002-9291-7654

M. Diez https://orcid.org/0000-0002-8334-3521

References

[1] Pitts R.A. *et al* 2019 *Nucl. Mater. Energy* **20** 100696
[2] Philipps V. *et al* 2011 *J. Nucl. Mater.* **415** S2
[3] Ueda Y., Coenen J.W., De Temmerman G., Doerner R.P., Linke J., Philipps V. and Tsitrone E. 2014 *Fusion Eng. Des.* **89** 901
[4] Brezinsek S. *et al* (WP PFC contributors) 2017 *Nucl. Fusion* **57** 116041
[5] Meyer H. *et al* (the EUROfusion MST1 Team) 2019 *Nucl. Fusion* **50** 112014
[6] Bourdelle C. *et al* (JET Contributors) 2015 *Nucl. Fusion* **55** 063017
[7] Brezinsek S. *et al* 2019 *Nucl. Fusion* **59** 096035
[8] Hakola A., Koivuranta S., Likonen J., Herrmann A., Maier H., Mayer M., Neu R. and Rohde V. 2015 *J. Nucl. Mater.* **463** 162
[9] Dux R. *et al* 2009 *J. Nucl. Mater.* **390–391** 858
[10] Guterl J., Wampler W.R., Rudakov D., Abrams T., Wang H.Q., McLean A.G. and Snyder P. 2019 *Plasma Phys. Control. Fusion* **61** 125015
[11] Herrmann A., Jaksic N., Leitenstern P., Greuner H., Krieger K., de Marné P., Oberkofler M., Rohde V. and Schall G. 2015 *Fusion Eng. Des.* **98–99** 1496
[12] Hakola A. *et al* 2016 *Phys. Scr.* **T167** 014026
[13] Brezinsek S. *et al* 2017 *Nucl. Mater. Energy* **12** 575
[14] Hakola A. *et al* (JET Contributors) 2017 *Nucl. Fusion* **57** 086019
[15] Hakola A. *et al* 2017 *Nucl. Mater. Energy* **12** 423
[16] Hakola A. *et al* 2020 *Nucl. Mater. Energy* **25** 100863
[17] Kirschner A., Philipps V., Winter J. and Kögler U. 2000 *Nucl. Fusion* **40** 989
[18] Wiesen S. *et al* 2015 *J. Nucl. Mater.* **463** 480
[19] Stangeby P.C. and Elder J.D. 1995 *Nucl. Fusion* **35** 1391
[20] Schmid K., Krieger K., Lisgo S.W., Meisl G. and Brezinsek S. 2015 *Nucl. Fusion* **55** 053015
[21] Balden M. *et al* 2021 *Phys. Scr.* **96** 124020
[22] Gallo A. *et al* 2020 *Phys. Scr.* **T171** 014013
[23] Bufferand H. *et al* 2015 *Nucl. Fusion* **55** 053025
[24] Brezinsek S. *et al* 2021 The competition between metallic nanostructures formation, erosion and co-deposition in He plasmas of the tokamaks EAST, WEST, and ASDEX Upgrade *24th Int. Conf. Plasma Surface Interactions in Controlled Fusion Devices (PSI 2020)* (Jeju, Korea, 25–29 January 2021) (https://mmm2020.kr/download/program/22_FI22(B).pdf)
[25] Tsitrone E. *et al* 2021 Investigation of plasma wall interactions between tungsten plasma facing components and helium plasmas in the WEST tokamak *28th IAEA Fusion Energy Conf.* (Nice, France 10–15 May 2021) (https://conferences.iaea.org/event/214/contributions/17455/)
[26] van Rooij G.J. *et al* 2020 *Phys. Scr.* **T171** 014060
[27] Hakola A. *et al* 2014 *Phys. Scr.* **T159** 014027
[28] Ding R. *et al* 2016 *Nucl. Fusion* **56** 016021
[29] Kirschner A., Tskhakaya D., Brezinsek S., Borodin D., Romazanov J., Ding R., Eksaeva A. and Linsmeier C. 2018 *Plasma Phys. Control. Fusion* **60** 014041
[30] Xie H., Ding R., Kirschner A., Chen J.L., Ding F., Mao H.M., Feng W., Borodin D. and Wang L. 2017 *Phys. Plasmas* **24** 092512
[31] Lahtinen A. *et al* 2017 Effect of surface roughness on erosion behaviour of tungsten divertor components on ASDEX Upgrade *44th European Physical Society Conference on Plasma Physics* (Belfast, the United Kingdom 26–30 June 2017) (http://ocs.ciemat.es/EPS2017PAP/pdf/P2.119.pdf)
[32] Eksaeva A. *et al* 2020 *Phys. Scr.* **T171** 014057
[33] Eksaeva A. *et al* 2021 *Nucl. Mater. Energy* **27** 100987
[34] Schmid K., Mayer M., Adelhelm C., Balden M. and Lindig S. 2010 *Nucl. Fusion* **50** 105004
[35] Mayer M., Rohde V., Ramos G., Vainonen-Ahlgren E., Likonen J. and Chen J.L. 2007 *Phys. Scr.* **T128** 106
[36] Krieger K. *et al* 2020 *Phys. Scr.* **T171** 014037
[37] Mayer M. *et al* 2020 *Phys. Scr.* **T171** 014035
[38] Hakola A., Likonen J., Koivuranta S., Krieger K., Mayer M., Neu R., Rohde V. and Sugiyama K. 2011 *J. Nucl. Mater.* **415** S227